Spin-orbit coupling driven crossover from a starfruitlike nodal semimetal to Dirac and Weyl semimetal state in CaAuAs

Bahadur Singh, Sougata Mardanya, Chenliang Su, Hsin Lin, Amit Agarwal, and Arun Bansil

Phys. Rev. B **98**, 085122 — Published 10 August 2018

DOI: 10.1103/PhysRevB.98.085122

Starfruit-like nodal semimetal to Dirac and Weyl semimetal state in CaAuAs

Bahadur Singh*†,[1,2] Sougata Mardanya*,[3] Chenliang Su,[1] Hsin Lin†,[4] Amit Agarwal†,[3] and Arun Bansil[2]

[1]*SZU-NUS Collaborative Center and International Collaborative Laboratory of 2D Materials for Optoelectronic Science & Technology, Engineering Technology Research Center for 2D Materials Information Functional Devices and Systems of Guangdong Province, College of Optoelectronic Engineering, Shenzhen University, ShenZhen 518060, China*

[2]*Department of Physics, Northeastern University, Boston, Massachusetts 02115, USA*

[3]*Department of Physics, Indian Institute of Technology - Kanpur, Kanpur 208016, India*

[4]*Institute of Physics, Academia Sinica, Taipei 11529, Taiwan*

Band-crossings that occur on a mirror plane are compelled to form nodal loops in the momentum space in the absence of spin-orbit coupling (SOC). When other equivalent mirror planes are present, multiple such nodal loops can combine to form interesting topological structures involving crossed nodal lines. Here, based on first-principles calculations and an effective **k.p** model analysis, we show that CaAuAs hosts a unique starfruit-like crossed-nodal-line structure in the bulk electronic dispersion, which is comprised of three nodal loops that cross each other at the time-reversal-invariant momentum point A. When the SOC is turned on, the nodal loops are gapped out, resulting in a stable Dirac semimetal state with a pair of Dirac points along the $\Gamma - A$ direction in the Brillouin zone. These Dirac points are protected by the combination of time-reversal, inversion, and C_3 rotation symmetries. We discuss how a systematic elimination of the symmetry constraints yields a Weyl semimetal and eventually a topological insulator state.

I. INTRODUCTION

Topological phases of quantum matter are currently at the forefront of condensed matter and materials sciences research[1–4]. The initial focus on insulating phases has shifted in the last few years to topological semimetals in which the bulk electronic spectrum hosts symmetry-protected gapless crossings near the Fermi level between the valence and conduction bands. Electronic states near the band-crossings mimic the Dirac and Weyl fermions familiar in the standard model of relativistic high-energy physics. The related Dirac and Weyl semimetals possess discrete four- and two-fold degenerate protected gapless points in their bulk spectra in which low energy excitations are Dirac[5–15] and Weyl fermions[16–26]. Under certain symmetry operations such as the mirror planes, these band-crossings can persist along one-dimensional (1D) loops, and give rise to nodal-line semimetals (NLSM)[27–48]. In contrast to Dirac and Weyl semimetals, energy dispersion in the NLSMs is quadratic in momentum along the direction tangential to the nodal line and linear along the other two perpendicular directions. Low-energy excitations in the NLSMs with highly anisotropic energy dispersions do not have any high-energy counterparts. Nontrivial bulk band topologies of topological semimetals are also associated with 2D surface states with open Fermi surfaces in the Weyl semimetals and flat drumhead-like Fermi surfaces in the NLSMs. The unique bulk and surface states of topological semimetals provide a new platform for investigating various intriguing high-energy and relativistic physics phenomena in table-top experiments and an exciting basis for developing next-generation technological applications[1–4].

Among the topological semimetals, the NLSMs are perhaps more interesting because of their high density of states (DOS) at the Fermi level, which could drive exotic correlation physics in these materials[48,49]. The nontrivial band structure of NLSMs leads to magnetic, optical, and transport properties that are distinctly different from those of Weyl and Dirac semimetals. NLSMs have been theoretically proposed in various families of compounds and experimentally verified recently in $PbTaSe_2$, CaAgAs, and ZrSi(S,Te)[31–34,50–52]. A focus of research has been the stability of nodal-line crossings with respect to the strength of the SOC, whose presence usually unlocks nodal loops to yield various topological states such as the Dirac and Weyl semimetals and the fully gapped insulators. Moreover, since nodal lines are enforced by mirror symmetries, they can form interesting crossed-nodal-line connections in the presence of multiple mirror planes[44–47].

In this paper, we discuss the topological NLSM state and its transition to the Dirac and Weyl semimetal states in ternary hexagonal CaAuAs using first-principles calculations and a **k.p** model Hamiltonian analysis. We show that CaAuAs realizes a unique crossed-nodal-lines semimetal state, which is composed of three nodal loops in the absence of SOC. The nodal loops are located on the vertical mirror symmetry planes of the D^4_{6h} symmetry group and intersect at the A point of the Brillouin zone (BZ), forming starfruit-like nodal crossings. A similar crossed-nodal-lines state has been reported recently in YH_3[47] and LiAuSe[53]. Inclusion of the SOC gaps out

*These authors contributed equally to this work.
†Corresponding authors' emails: bahadursingh24@gmail.com, nilnish@gmail.com, amitag@iitk.ac.in

the nodal loops and transitions the system into a stable, symmetry-protected Dirac semimetal state with a pair of Dirac points, which are located along the C_3 rotation axis. We also characterize the topological state of CaAuAs through surface-state calculations. It is well known that Dirac semimetals lie adjacent to a variety of gapped as well as semimetal phases. Accordingly, we have investigated topological transitions in CaAuAs when C_3 rotational and time-reversal symmetries are broken.

The remainder of this paper is organized as follows. In Sec. II, we describe computational details and discuss the crystal structure and symmetry properties of CaAuAs. Sec. III discusses the starfruit-like NLSM state. In Sec. IV, we present an analysis of the SOC-induced Dirac semimetal state. The topological surface electronic structure is also explored. In Sec. V, we present an effective **k.p** Hamiltonian. Effects of selective symmetry-breaking and the emergence of topological insulator and Weyl semimetal states are discussed in Sec. VI. In Sec. VII, we discuss the topological band structure of the CaAuAs materials family more generally. Finally, we summarize our findings in Sec. VIII.

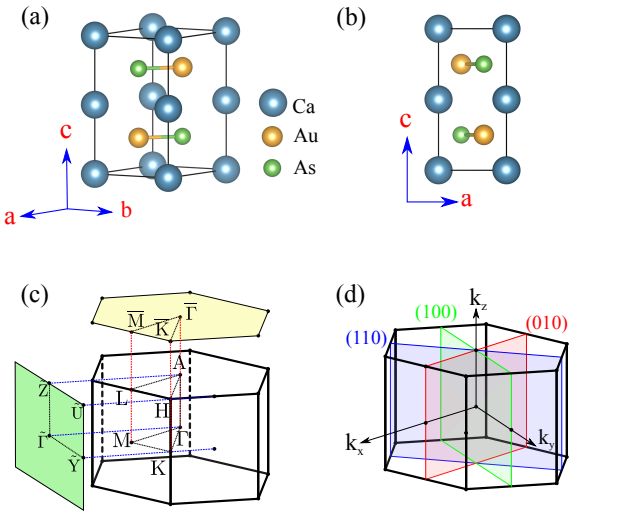

FIG. 1: (a) Side and (b) (010) view of the crystal structure of CaAuAs. (c) Bulk BZ and its projection onto the (001) and (010) surface planes. The relevant bulk and surface high-symmetry points are marked. (d) Illustration of three mirror-reflection planes m_{100} (red), m_{010} (green) and m_{110} (blue) in the bulk BZ.

II. METHODOLOGY AND CRYSTAL STRUCTURE

Electronic structure calculations were performed within the framework of the density functional theory (DFT) with the projector augmented wave (PAW) pseudopotentials[54], as implemented in the Vienna *ab initio* simulation package (VASP)[55,56]. The generalized gradient approximation with the Perdew-Burke-Ernzerhof parameterization was used to include exchange-correlation effects[57]. Bulk calculations used a plane wave energy cut-off of 500 eV and a $20 \times 20 \times 20$ Γ-centered $k-$mesh to sample the BZ[58]. Total energies were converged to 10^{-7} eV. The SOC was used self-consistently to incorporate relativistic effects. Experimental lattice parameters of CaAuAs ($a = b = 4.388\mathring{A}$ and $c = 7.925\mathring{A}$) were used. Topological properties were calculated by employing a tight-binding model obtained by using the WannierTools[59,60]. VESTA software package was used for crystal structure visualization[61].

CaAuAs crystallizes in the hexagonal crystal lattice with space group D^4_{6h} (No. 194). The primitive unit cell and its (010) view are shown in Fig. 1. The unit cell contains six atoms (two Ca, two Au, and two As), which occupy Wyckoff positions 2a, 2d, and 2d. The crystal structure can be viewed as a shared honeycomb lattice of Au and As atoms that are stacked along the hexagonal z-axis. The hexagonal Ca layers are inserted in this stacking sequence while maintaining the bulk inversion symmetry. The bulk BZ and the associated surface-projected BZs are shown in Fig. 1(c). The crystal has three equivalent mirror-reflection planes m_{110}, m_{100}, and m_{010}, which are illustrated in Fig. 1(d).

III. A STARFRUIT-LIKE NODAL-LINE SEMIMETAL

Electronic structure of CaAuAs without the SOC is shown in Fig. 2. Band-crossings in inversion symmetric solids usually occur on high-symmetry lines or planes. The stability of these crossings against 'band repulsion' arises from the fact that the bands that are crossing belong to different irreducible representations of the space group. In particular, on a mirror symmetry plane, if the two bands involved have opposite mirror eigenvalues, then they are constrained by this symmetry to form a stable nodal loop. These nodal lines, which appear on equivalent mirror planes, can easily get connected at high-symmetry points or intersection of mirror planes to form crossed-nodal-line structures.

Figure 2(a) shows the band structure of CaAuAs along selected directions in the bulk BZ. A symmetry analysis shows that, near the Fermi energy, the valence and conduction bands at Γ belong to E_{2g} and E_{1u} representations of the D_{6h} point group, respectively. These bands have opposite mirror eigenvalues and cross along the $\Gamma - M$ direction as shown in the closeups of Figs. 2(b) and (d). Note that the $\Gamma - M$ is an irreducible line associated with the three equivalent mirror planes highlighted in Fig. 1(d). A careful analysis reveals that this band crossing persists along the mirror plane to form a closed loop. Further exploration of the 3D band structure shows the presence of similar nodal lines on the m_{010} and m_{110} mirror planes, see Fig. 2(c). These equivalent nodal loops cross at the high-symmetry point $A = (0, 0, \pm\pi)$ to form a starfruit-like nodal structure [see Fig. 2(c)].[63] CaAuAs also exhibits a C_3 rotation-symmetry-protected

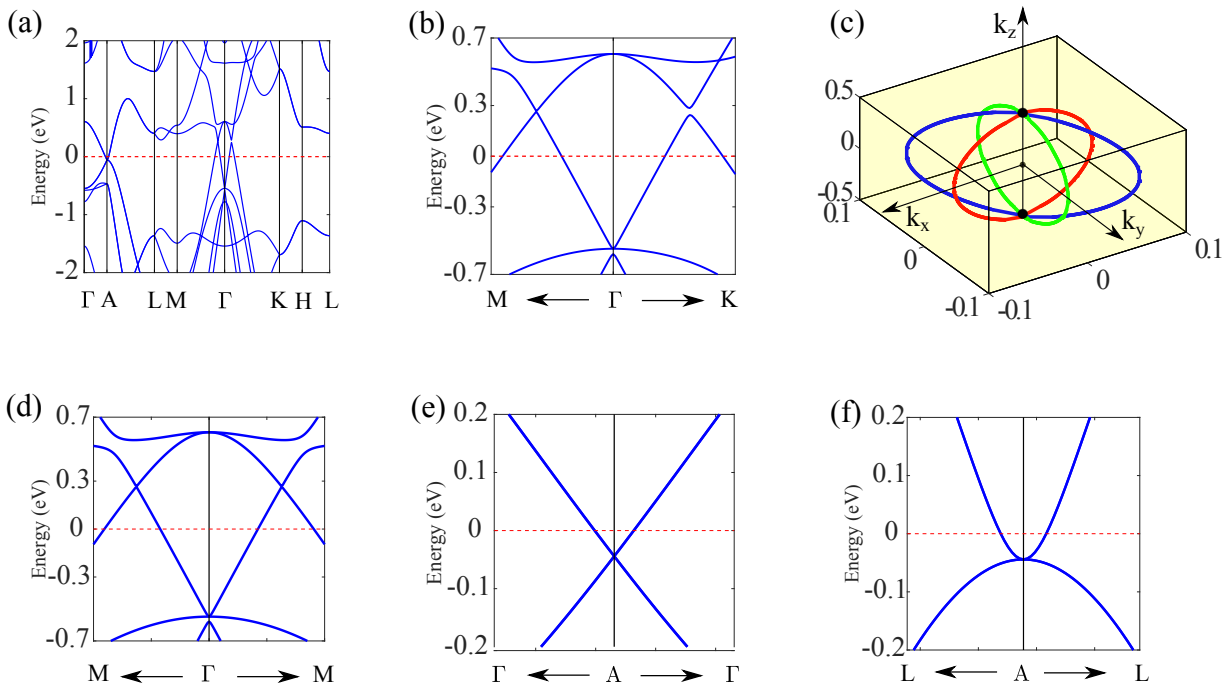

FIG. 2: (a) Electronic band structure of CaAuAs along the high-symmetry directions in the BZ without SOC. (b),(d) Closeups of the band-structure along the $M-\Gamma-K$ path. A linearly dispersing gapless point, which lies on the m_{100} mirror plane, is evident along the $\Gamma-M$ direction around 0.26 eV. (c) Configuration of nodal lines in the full BZ. Nodal lines located on the three equivalent mirror planes are seen to cross at the $\pm A$ point. (e),(f) Energy dispersion in the vicinity of the A point: It is linear along the $\Gamma-A$ (k_z) direction and non-linear in the $L-A$ (k_x, k_y) directions.

Dirac point at the A-point with a unique eight-fold degeneracy without the SOC; the band dispersion around this point is anisotropic, being linear along the $\Gamma-$A direction and non-linear along the in-plane A$-$L direction, see Figs. 2(e) and (f).

IV. SPIN-ORBIT COUPLING INDUCED DIRAC SEMIMETAL

In the absence of non-symmorphic symmetries, the SOC can gap nodal lines and drive changes in band topologies. In order to delineate effects of the SOC, we present the band structure of CaAuAs including the SOC in Fig. 3. The nodal line crossings are now gapped, generating a clear bandgap at the band crossing points, see Figs. 3(b) and (d). However, in contrast to ZrPtGe or ZrSiS[48,51,52,62], here the band crossing is retained only along the C_3 rotation axis ($\Gamma-$A direction) at $\pm\mathbf{k}_D$ [see Fig. 3(e)]. Owing to the presence of both inversion and time-reversal symmetries, the $\pm\mathbf{k}_D$ points are four-fold degenerate with a linear dispersion along all three directions [Figs. 3(e) and (f)]. A careful symmetry analysis shows that the crossing bands belong to different irreducible representations (Γ_7^- and Γ_9^+) with opposite parities and different C_3 rotational eigenvalues. These nodal points are thus unavoidable and protected by the C_3 rotational symmetry. Keeping in mind that the bandgap is typically underestimated in the GGA, we have also computed the band structure using the hybrid exchange-correlation functional to confirm the presence of the aforementioned Dirac semimetal state with a pair of Dirac cones (not shown for brevity). These results demonstrate that CaAuAs realizes a robust, nearly ideal type-I Dirac semimetal in which the Dirac points lie close to the Fermi level, much like the case of Na_3Bi. The transition from a nodal-chain semimetal to a Dirac semimetal with SOC is illustrated in Figs. 3(g) and (h).

The nontrivial bulk band topology is accompanied by the existence of topological surface states. In order to showcase these states and their connection to the bulk bands, we present the (001) and (010) surface band structure of CaAuAs in Fig. 4. On the (001) surface, a pair of Dirac points located on the $\Gamma-A$ bulk direction projects onto the surface $\overline{\Gamma}$ point, see Fig. 4(a). In addition to these projected bulk Dirac cones, we find topological states that connect the valence and conduction bands as in the case of a topological insulator. These states result from the inverted bulk band structure and may be considered a precursor of the metallic surface states in a topological insulator. Figures 4(b) and 4(c) show the constant energy cuts at the Fermi energy (E_f) and the energy of the Dirac point (E_D), respectively. The projected Dirac points are seen at the $\overline{\Gamma}$ in Fig. 4(c).

Figure 4(d) shows the band structure of the (010) sur-

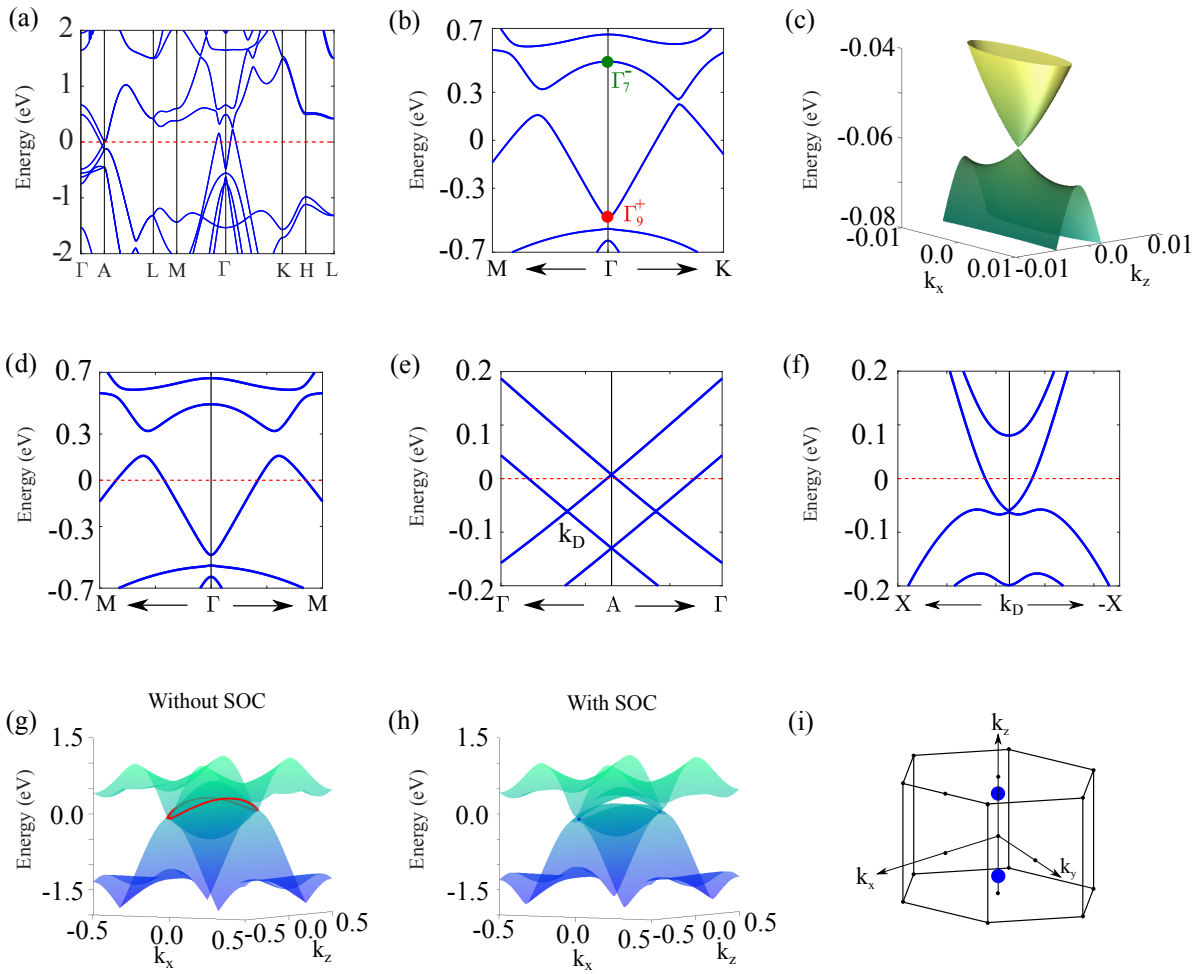

FIG. 3: (a) Electronic band structure of CaAuAs with SOC. (b),(d) Closeups of the band structure along the high-symmetry directions. A clear band gap emerges at the band-crossings without the SOC on the mirror-symmetric $\Gamma - M$ line. (e) Energy dispersion along the $\Gamma - A$ line displaying a pair of Dirac points at $\pm\mathbf{k}_D$; dispersion along an in-plane direction is shown in (f). (c) A 3D rendition of the Dirac cone in the $E - k_x - k_z$ space. A linear dispersion along the three principal directions confirms that this is a type-I Dirac cone. (g) 3D dispersion of a single nodal line on the m_{010} mirror plane without the SOC. When the SOC is included, the nodal line is gapped, leaving a pair of unavoidable crossings on the C_3 rotation axis as seen in (h). (i) Blue markers show the location of the Dirac points in the BZ.

face. The pair of Dirac points on this surface project onto the $\tilde{\Gamma} - \tilde{Z}$ surface direction [see Fig. 1(c)]. Surface states are seen to emerge from the Dirac node, suggesting the existence of double Fermi arc states over this surface.[64] Note that a Dirac point is a stable merger of two Weyl points of opposite chiral charge in the presence of a crystalline symmetry. Therefore, double Fermi arcs may connect a pair of Dirac nodes, forming a closed surface loop mediated by the Dirac nodes. Figs. 4(e) and 4(f) show constant energy contours at $E = E_f$ and $E = E_D$, respectively. We can clearly see a pair of Fermi arcs terminated on the Dirac nodes in 4(f). They emerge from one Dirac node along the $\tilde{\Gamma} - \tilde{Z}$ direction and terminate on the other. The evolution of these Fermi arc states at a higher energy is shown in Fig. 4(e).

V. EFFECTIVE HAMILTONIAN

We now discuss a low-energy **k.p** effective model Hamiltonian, which is derived using the theory of invariants in a manner similar to Na_3Bi[12] and LiAuSe[53]. As already noted above, the irreducible representations of the two bands crossing at Γ are Γ_7^- and Γ_9^+ in which the major contribution is from As-p and Au-s orbitals, respectively. Here, the superscript $(+)$ or $(-)$ represents parity of the state. In the presence of SOC, a 4×4 effective Hamiltonian in the basis $|s^+_{\frac{1}{2}}, \frac{1}{2}\rangle$, $|p^-_{\frac{3}{2}}, \frac{3}{2}\rangle$, $|s^+_{\frac{1}{2}}, -\frac{1}{2}\rangle$,

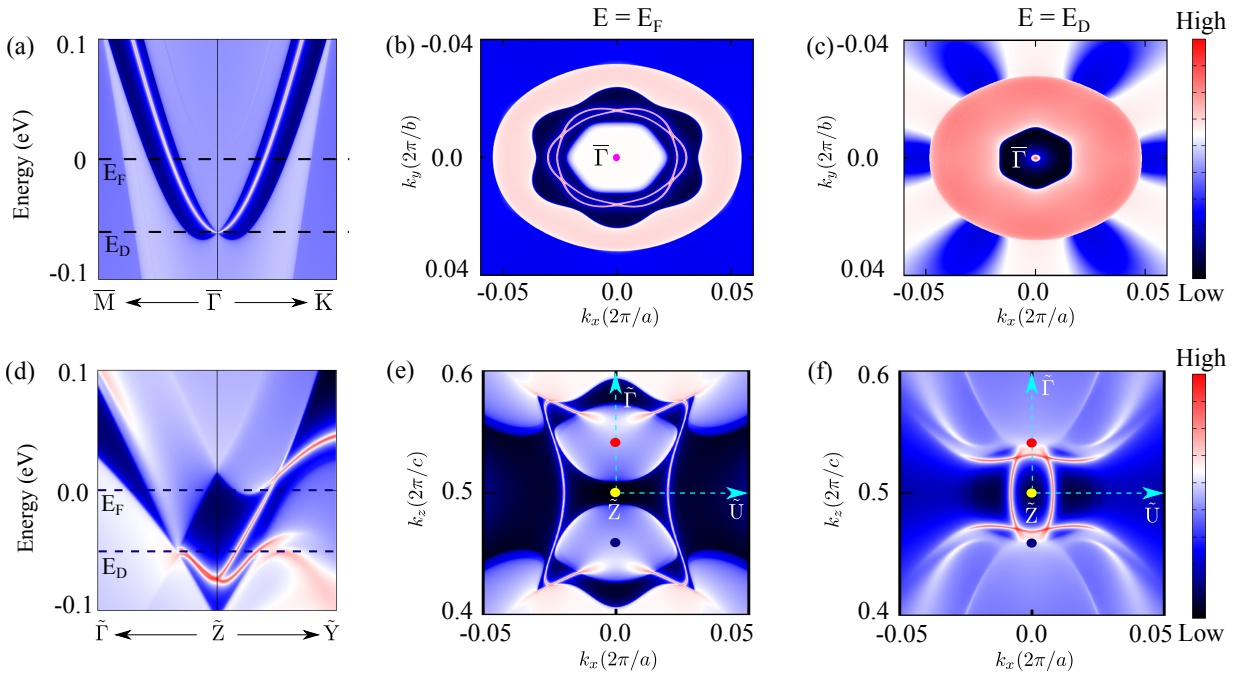

FIG. 4: (a) Band structure of (001) surface of CaAuAs including SOC. The shaded blue region marks projected bulk bands, and sharp lines identify the surface states. Constant energy contours at (b) $E = E_f$ and (c) $E = E_D$; these energies are marked with dashed lines in (a). (d-f) Same as (a-c) but for (010) surface. The surface states in (d) emanate at the Dirac point along the $\tilde{\Gamma} - \tilde{Z}$ direction. The double-Fermi-arc states connecting the pair of Dirac points are evident in (e) and (f).

$|p^-_{\frac{3}{2}}, -\frac{3}{2}\rangle$ with the constraints of D^4_{6h} symmetries is,

$$H_\Gamma(\mathbf{k}) = \epsilon(\mathbf{k}) + \begin{pmatrix} M(\mathbf{k}) & A(\mathbf{k})\mathbf{k}_+ & 0 & -B^*(\mathbf{k}) \\ A(\mathbf{k})\mathbf{k}_- & -M(\mathbf{k}) & B^*(\mathbf{k}) & 0 \\ 0 & B(\mathbf{k}) & M(\mathbf{k}) & A(\mathbf{k})\mathbf{k}_- \\ -B(\mathbf{k}) & 0 & A(\mathbf{k})\mathbf{k}_+ & -M(\mathbf{k}) \end{pmatrix} . \quad (1)$$

Here, $\mathbf{k}_\pm = k_x \pm ik_y$, $\epsilon(\mathbf{k}) = c_0 + c_1 k_z^2 + c_2(k_x^2 + k_y^2)$, $A(\mathbf{k}) = A_0 + A_1 k_z^2 + A_2(k_x^2 + k_y^2)$, $B(\mathbf{k}) = B_3 k_z k_+^2$, and $M(\mathbf{k}) = -M_0 + M_1 k_z^2 + M_2(k_x^2 + k_y^2)$ with M_0, M_1, and $M_2 > 0$ to ensure a band inversion. The associated energy dispersion of this Hamiltonian is,

$$E(\mathbf{k}) = \epsilon(\mathbf{k}) \pm \sqrt{M(\mathbf{k})^2 + A(\mathbf{k})^2 k_+ k_- + |B(\mathbf{k})|^2} , \quad (2)$$

with a pair of gapless Dirac points located on the $\Gamma - A$ line at $\pm\mathbf{k}_D = (0, 0, \pm\sqrt{M_0/M_1})$. By neglecting the higher order terms in $B(k) = B_3 k_z k_+^2$ and $A(\mathbf{k})$, one can obtain a linearized massless Dirac Hamiltonian around each gapless point. By fitting the energy dispersion of Eq. 2 with our first-principles results on CaAuAs, we obtain the fitting parameters: $c_0 = -0.05$ eV , $c_1 = -0.161$ eV Å^2, $c_2 = 13.127$ eV Å^2, $M_0 = 0.348$ eV, $M_1 = 2.722$ eV Å^2, $M_2 = 13.452$ eV Å^2, $A_0 = 1.182$ eV, $A_1 = 4.236$ eV Å^2, $A_2 = -15.598$ eV Å^2 and $B_3 = 0.0004$ eV Å^4.

VI. BROKEN-SYMMETRY-INDUCED TOPOLOGICAL STATES IN CaAuAs

Recall that a Dirac semimetal can be thought of as providing a bridge to a variety of topological phases, which can be obtained when the underlying symmetries are broken. We have shown above that the Dirac points in CaAuAs are protected by the C_3 rotation symmetry in an inversion- and time-reversal symmetric environment. We now discuss the novel physics that could be realized by breaking these symmetries in CaAuAs.

A. Topological insulator

Breaking the C_3 rotational symmetry in CaAuAs introduces an additional linear leading order term in $B(\mathbf{k}) = B_1 k_z$ in Eq. 1, which ensures gap opening at the Dirac points. To confirm this effect independently, we applied a compressive in-plane strain by varying the angle between the in-plane hexagonal lattice vectors from 120° to 116° in our *ab-initio* calculations. This breaks the C_3 symmetry, and indeed leads to a gap at the Dirac points as shown in Fig. 5(a). Since Dirac semimetal state in CaAuAs arises through a bulk band inversion, the C_3 symmetry-broken state could realize a topological insulator with Dirac cone surface states. In Fig. 5(b) we show the energy dispersion of (001) surface, which confirms that this is in fact the case with the presence of a

single Dirac cone that spans the bulk energy spectrum.

B. Topological Weyl semimetal

Weyl states are the most robust states among the topological semimetals in the sense that they rely only on the translation invariance of the crystal. In CaAuAs, the Weyl semimetal state can be realized by breaking either the inversion or the time-reversal symmetry. Here, we illustrate this evolution of the Dirac semimetal through the breaking of the time-reversal symmetry by introducing a Zeeman field along the z direction in the low-energy Hamiltonian. The model Hamiltonian of Eq. (1) with the Zeeman field is:

$$H_{\rm WSM}(\mathbf{k}) = H_{\Gamma}(\mathbf{k}) + h\sigma_z\tau_z. \quad (3)$$

Here, the second term describes the effective Zeeman field with strength h. As a result, each Dirac node at $k_{\rm D} = (0, 0, \pm\sqrt{M_0/M_1})$ with four-fold band degeneracy is found to split into a pair of Weyl points as shown in Fig. 5(c). These Weyl points appear along the $\Gamma - A$ direction at $\pm k_{\rm W}^{\pm} = (0, 0, \sqrt{(M_0 \pm h)/M_1})$.

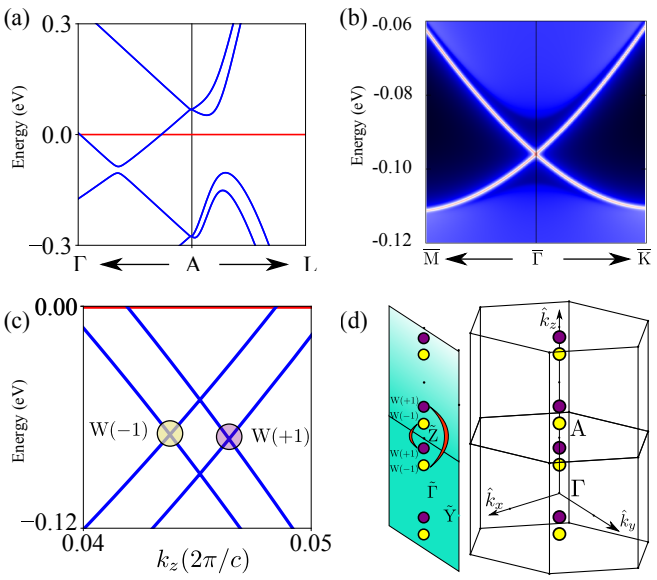

FIG. 5: (a) Bulk band structure of CaAuAs when the C_3 rotational symmetry is broken. A small band gap appears at the Dirac point along the $\Gamma - A$ direction. The associated surface energy spectrum is shown in (b). The topological surface Dirac cone is seen within the bulk band gap. (c) Bulk band structure of CaAuAs in the reduced k_z direction with the Zeeman field $h = 0.02$ eV in Eq. (3). A pair of Weyl points with opposite chiral charges is seen to emerge. (d) A schematic of the location of Weyl points and the Fermi-arc surface states in the bulk and surface BZs.

In order to evaluate the chirality associated with each of the four aforementioned Weyl nodes, we consider our effective Hamiltonian $H_{\rm WSM}$ in the vicinity of the Weyl points. Neglecting the fourth order off-diagonal terms in Eq. (3), the upper diagonal block can be expressed as

$$H^{(2\times2)}_{\rm WSM}(\mathbf{k}) = f_0(\mathbf{k})\mathbb{I} + f_1(\mathbf{k})\sigma_1 + f_2(\mathbf{k})\sigma_2 + f_3(\mathbf{k})\sigma_3\ . \quad (4)$$

Here, $\mathbb{I}$ is the 2×2 identity matrix, σ_i denote the three Pauli matrices, $f_0(\mathbf{k}) = \epsilon(\mathbf{k})$, $f_1(\mathbf{k}) = A(\mathbf{k})k_x$, $f_2(\mathbf{k}) = -A(\mathbf{k})k_y$ and $f_3(\mathbf{k}) = M(\mathbf{k}) + h$. This Hamiltonian results in a pair of gapless crossings at $\pm\mathbf{k}_{\rm W}^{-} = \pm\left(0, 0, \sqrt{\frac{M_0-h}{M_1}}\right)$. By carrying out a wave-vector expansion in the vicinity of each Weyl node, i.e $\mathbf{k} \to \pm\mathbf{k}_{\rm W}^{-} + \delta\mathbf{k}$, we obtain

$$H^{(2\times2)}_{\rm WSM}(\mathbf{k}) \approx f_0(\pm\mathbf{k}_{\rm W}^{-})\mathbb{I} + \mathbf{v}_0.\delta\mathbf{k}\mathbb{I} + \sum_{a=1,2,3}(\mathbf{v}_a.\delta\mathbf{k})\,\sigma_a\ , \quad (5)$$

where the three component vector $\mathbf{v}_j = \nabla_{\mathbf{k}} f_j(\mathbf{k})|_{\mathbf{k}=\pm\mathbf{k}_{\rm W}^{-}}$ with $j = 0, 1, 2, 3$. The chirality of each Weyl node is given by $C = sign(\mathbf{v}_x.\mathbf{v}_y \times \mathbf{v}_z)$[3]. In CaAuAs, we find the chirality of Weyl points located at $(+k_{\rm W}^{+}, +k_{\rm W}^{-}, -k_{\rm W}^{-}, -k_{\rm W}^{+})$ to be $(+1, -1, +1, -1)$, which is shown in Fig. 5(d). The Fermi arcs associated with each Dirac node thus naturally provide the Fermi arcs connecting a pair of Weyl nodes as illustrated schematically in Fig. 5(d).

VII. BAND STRUCTURE OF THE CaAuAs MATERIALS FAMILY MORE GENERALLY

Figure 6 shows that the bulk band structure of four other members of the CaAuAs materials family is similar to that of CaAuAs. Our analysis further indicates that all these materials support a starfruit-like crossed-nodal-lines topological structure without the SOC, and transition to a Dirac semimetal with the inclusion of SOC. It should be noted that the specifics of energy and $k-$space locations of the Dirac nodes are material dependent. Also, we expect that like CaAuAs, when various symmetry constraints are removed, these materials will yield other interesting topological states.

VIII. CONCLUSION

Based on our first-principles calculations and an effective low-energy model Hamiltonian analysis, we predict that CaAuAs hosts a unique starfruit-like crossed-nodal-lines semimetal state in the absence of the SOC. This topological state is formed by three equivalent nodal loops, which intersect at high-symmetry points lying on the k_z axis. When the SOC is turned on, the nodal lines are gapped out, and CaAuAs realizes a C_3 rotation-symmetry-protected Dirac semimetal with a pair of Dirac cones that exhibit linear dispersion along all momentum directions. The surface spectrum reveals the existence

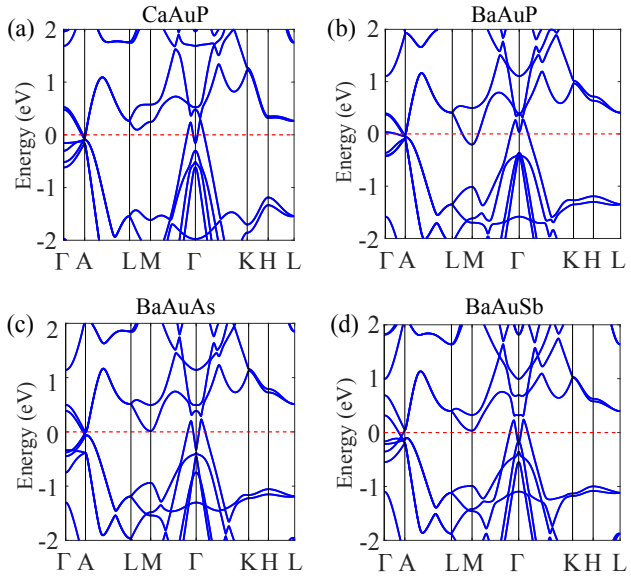

FIG. 6: Bulk band structure of the CaAuAs materials family with SOC. (a) CaAuP, (b) BaAuP, (c) BaAuAs, and (d) BaAuSb.

of a pair of double Fermi arc states, which connect the projections of the bulk Dirac cones over the surface. We also discuss how a variety of topological states emerge from the Dirac semimetal when various symmetries are broken. In particular, we show that the breaking of C_3 rotational symmetry drives CaAuAs into a topological insulating state, while breaking of the time-reversal symmetry leads to a Weyl semimetal with two pairs of Weyl nodes. Finally, we show that the topological band structure of several other members of the CaAuAs family is similar to that of CaAuAs. We thus conclude that CaAuAs materials family offers an interesting platform for investigating various exotic phenomena in topological materials.

ACKNOWLEDGMENTS

Work at the ShenZhen university is financially supported by the Shenzhen Peacock Plan (Grant No. 827-000113, KQTD2016053112042971), Science and Technology Planning Project of Guangdong Province (2016B050501005), and the Educational Commission of Guangdong Province (2016KSTCX126). The work at Northeastern University was supported by the US Department of Energy (DOE), Office of Science, Basic Energy Sciences grant number DE-FG02-07ER46352, and benefited from Northeastern University's Advanced Scientific Computation Center and the National Energy Research Scientific Computing Center through DOE grant number DE-AC02-05CH11231.

[1] A. Bansil, H. Lin, and T. Das, Rev. Mod. Phys. **88**, 021004 (2016).
[2] M. Z. Hasan and C. L. Kane, Rev. Mod. Phys. **82**, 3045 (2010).
[3] N. P. Armitage, E. J. Mele, and A. Vishwanath, Rev. Mod. Phys. **90**, 015001 (2018).
[4] D. Kong and Y. Cui, Nat. Chem. **3**, 845 (2011).
[5] S. M. Young, S. Zaheer, J. C. Y. Teo, C. L. Kane, E. J. Mele, and A. M. Rappe, Phys. Rev. Lett. **108**, 140405 (2012).
[6] S. M. Young and C. L. Kane, Phys. Rev. Lett. **115**, 126803 (2015).
[7] B. J. Wieder, Y. Kim, A. M. Rappe, and C. L. Kane, Phys. Rev. Lett. **116**, 186402 (2016).
[8] Z. K. Liu, B. Zhou, Y. Zhang, Z. J. Wang, H. M. Weng, D. Prabhakaran, S.-K. Mo, Z. X. Shen, Z. Fang, X. Dai, Z. Hussain, and Y. L. Chen, Science **343**, 864 (2014).
[9] Z. K. Liu, J. Jiang, B. Zhou, Z. J. Wang, Y. Zhang, H. M. Weng, D. Prabhakaran, S.-K. Mo, H. Peng, P. Dudin, T. Kim, M. Hoesch, Z. Fang, X. Dai, Z. X. Shen, D. L. Feng, Z. Hussain, and Y. L. Chen, Nature Materials **13**, 677 (2014).
[10] M. Neupane, S.-Y. Xu, R. Sankar, N. Alidoust, G. Bian, C. Liu, I. Belopolski, T.-R. Chang, H.-T. Jeng, H. Lin, A. Bansil, F. Chou, and M. Z. Hasan, Nature Communications **5**, 3786 (2014).
[11] S. Borisenko, Q. Gibson, D. Evtushinsky, V. Zabolotnyy, B. Büchner, and R. J. Cava, Phys. Rev. Lett. **113**, 027603 (2014).
[12] Z. Wang, Y. Sun, X.-Q. Chen, C. Franchini, G. Xu, H. Weng, X. Dai, and Z. Fang, Phys. Rev. B **85**, 195320 (2012).
[13] Z. Wang, H. Weng, Q. Wu, X. Dai, and Z. Fang, Phys. Rev. B **88**, 125427 (2013).
[14] X. Zhang, Z.-M. Yu, X.-L. Sheng, H. Y. Yang, and S. A. Yang, Phys. Rev. B **95**, 235116 (2017).
[15] C. Chen, S.-S. Wang, L. Liu, Z.-M. Yu, X.-L. Sheng, Z. Chen, and S. A. Yang, Phys. Rev. Materials **1**, 044201 (2017).
[16] S.-Y. Xu, I. Belopolski, N. Alidoust, M. Neupane, G. Bian, C. Zhang, R. Sankar, G. Chang, Z. Yuan, C.-C. Lee, S.-M. Huang, H. Zheng, J. Ma, D. S. Sanchez, B. Wang, A. Bansil, F. Chou, P. P. Shibayev, H. Lin, S. Jia, and M. Z. Hasan, Science **349**, 613 (2015).
[17] S.-M. Huang, S.-Y. Xu, I. Belopolski, C.-C. Lee, G. Chang, B. Wang, N. Alidoust, G. Bian, M. Neupane, C. Zhang, S. Jia, A. Bansil, H. Lin, and M. Z. Hasan, Nature Communications **6**, 7373 (2015).
[18] B. Q. Lv, H. M. Weng, B. B. Fu, X. P. Wang, H. Miao, J. Ma, P. Richard, X. C. Huang, L. X. Zhao, G. F. Chen, Z. Fang, X. Dai, T. Qian, and H. Ding, Phys. Rev. X **5**, 031013 (2015).
[19] S.-Y. Xu, N. Alidoust, I. Belopolski, Z. Yuan, G. Bian, T.-R. Chang, H. Zheng, V. N. Strocov, D. S. Sanchez, G. Chang, C. Zhang, D. Mou, Y. Wu, L. Huang, C.-C. Lee, S.-M. Huang, B. Wang, A. Bansil, H.-T. Jeng, T. Neupert, A. Kaminski, H. Lin, S. Jia, and M. Zahid Hasan, Nature Physics **11**, 748 (2015).

[20] G. Xu, H. Weng, Z. Wang, X. Dai, and Z. Fang, Phys. Rev. Lett. **107**, 186806 (2011).
[21] C. Fang, M. J. Gilbert, X. Dai, and B. A. Bernevig, Phys. Rev. Lett. **108**, 266802 (2012).
[22] H. Weng, C. Fang, Z. Fang, B. A. Bernevig, and X. Dai, Phys. Rev. X **5**, 011029 (2015).
[23] B. Singh, A. Sharma, H. Lin, M. Z. Hasan, R. Prasad, and A. Bansil, Phys. Rev. B **86**, 115208 (2012).
[24] T.-R. Chang, S.-Y. Xu, D. S. Sanchez, W.-F. Tsai, S.-M. Huang, G. Chang, C.-H. Hsu, G. Bian, I. Belopolski, Z.-M. Yu, S. A. Yang, T. Neupert, H.-T. Jeng, H. Lin, and M. Z. Hasan, Phys. Rev. Lett. **119**, 026404 (2017).
[25] C.-K. Chiu and A. P. Schnyder, Phys. Rev. B **90**, 205136 (2014).
[26] Z. Gao, M. Hua, H. Zhang, and X. Zhang, Phys. Rev. B **93**, 205109 (2016).
[27] C. Fang, H. Weng, X. Dai, and Z. Fang, Chinese Physics B **25**, 117106 (2016).
[28] A. A. Burkov, M. D. Hook, and L. Balents, Phys. Rev. B **84**, 235126 (2011).
[29] M. Phillips and V. Aji, Phys. Rev. B **90**, 115111 (2014).
[30] C. Fang, Y. Chen, H.-Y. Kee, and L. Fu, Phys. Rev. B **92**, 081201 (2015).
[31] G. Bian, T.-R. Chang, R. Sankar, S.-Y. Xu, H. Zheng, T. Neupert, C.-K. Chiu, S.-M. Huang, G. Chang, I. Belopolski, D. S. Sanchez, M. Neupane, N. Alidoust, C. Liu, B. Wang, C.-C. Lee, H.-T. Jeng, C. Zhang, Z. Yuan, S. Jia, A. Bansil, F. Chou, H. Lin, and M. Z. Hasan, Nature Communications **7**, 10556 (2016).
[32] M. Neupane, I. Belopolski, M. M. Hosen, D. S. Sanchez, R. Sankar, M. Szlawska, S.-Y. Xu, K. Dimitri, N. Dhakal, P. Maldonado, P. M. Oppeneer, D. Kaczorowski, F. Chou, M. Z. Hasan, and T. Durakiewicz, Phys. Rev. B **93**, 201104 (2016).
[33] L. M. Schoop, M. N. Ali, C. Straßer, A. Topp, A. Varykhalov, D. Marchenko, V. Duppel, S. S. P. Parkin, B. V. Lotsch, and C. R. Ast, Nature Communications **7**, 11696 (2016).
[34] A. Yamakage, Y. Yamakawa, Y. Tanaka, and Y. Okamoto, Journal of the Physical Society of Japan **85**, 013708 (2015).
[35] L. S. Xie, L. M. Schoop, E. M. Seibel, Q. D. Gibson, W. Xie, and R. J. Cava, APL Materials **3**, 083602 (2015).
[36] Y. Kim, B. J. Wieder, C. L. Kane, and A. M. Rappe, Phys. Rev. Lett. **115**, 036806 (2015).
[37] K. Mullen, B. Uchoa, and D. T. Glatzhofer, Phys. Rev. Lett. **115**, 026403 (2015).
[38] H. Weng, Y. Liang, Q. Xu, R. Yu, Z. Fang, X. Dai, and Y. Kawazoe, Phys. Rev. B **92**, 045108 (2015).
[39] R. Yu, H. Weng, Z. Fang, X. Dai, and X. Hu, Phys. Rev. Lett. **115**, 036807 (2015).
[40] Y. Chen, Y. Xie, S. A. Yang, H. Pan, F. Zhang, M. L. Cohen, and S. Zhang, Nano Letters **15**, 6974 (2015).
[41] R. Li, H. Ma, X. Cheng, S. Wang, D. Li, Z. Zhang, Y. Li, and X.-Q. Chen, Phys. Rev. Lett. **117**, 096401 (2016).
[42] Y.-J. Jin, R. Wang, J.-Z. Zhao, Y.-P. Du, C.-D. Zheng, L.-Y. Gan, J.-F. Liu, H. Xu, and S. Y. Tong, Nanoscale **9**, 13112 (2017).
[43] G. Bian, T.-R. Chang, H. Zheng, S. Velury, S.-Y. Xu, T. Neupert, C.-K. Chiu, S.-M. Huang, D. S. Sanchez, I. Belopolski, N. Alidoust, P.-J. Chen, G. Chang, A. Bansil, H.-T. Jeng, H. Lin, and M. Z. Hasan, Phys. Rev. B **93**, 121113 (2016).
[44] T. Bzduek, Q. Wu, A. Ruegg, M. Sigrist, and A. A. Soluyanov, Nature **538**, 75 (2016).
[45] G. Chang, S.-Y. Xu, X. Zhou, S.-M. Huang, B. Singh, B. Wang, I. Belopolski, J. Yin, S. Zhang, A. Bansil, H. Lin, and M. Z. Hasan, Phys. Rev. Lett. **119**, 156401 (2017).
[46] Z. Yan, R. Bi, H. Shen, L. Lu, S.-C. Zhang, and Z. Wang, Phys. Rev. B **96**, 041103 (2017).
[47] S. Kobayashi, Y. Yamakawa, A. Yamakage, T. Inohara, Y. Okamoto, and Y. Tanaka, Phys. Rev. B **95**, 245208 (2017).
[48] B. Singh, X. Zhou, H. Lin, and A. Bansil, Phys. Rev. B **97**, 075125 (2018).
[49] Y. Huh, E.-G. Moon, and Y. B. Kim, Phys. Rev. B **93**, 035138 (2016).
[50] D. Takane, K. Nakayama, S. Souma, T. Wada, Y. Okamoto, K. Takenaka, Y. Yamakawa, A. Yamakage, T. Mitsuhashi, K. Horiba, H. Kumigashira, T. Takahashi, and T. Sato, npj Quantum Materials **3**, 1 (2018).
[51] J. Hu, Z. Tang, J. Liu, X. Liu, Y. Zhu, D. Graf, K. Myhro, S. Tran, C. N. Lau, J. Wei, and Z. Mao, Phys. Rev. Lett. **117**, 016602 (2016).
[52] M. S. Lodge, G. Chang, C.-Y. Huang, B. Singh, J. Hellerstedt, M. T. Edmonds, D. Kaczorowski, M. M. Hosen, M. Neupane, H. Lin, M. S. Fuhrer, B. Weber, and M. Ishigami, Nano Letters **17**, 7213 (2017).
[53] C. Chen, Z. Su, X. Zhang, Z. Chen, and X.-L. Sheng, The Journal of Physical Chemistry C **121**, 28587 (2017).
[54] P. E. Blöchl, Phys. Rev. B **50**, 17953 (1994).
[55] G. Kresse and J. Furthmüller, Phys. Rev. B **54**, 11169 (1996).
[56] G. Kresse and D. Joubert, Phys. Rev. B **59**, 1758 (1999).
[57] J. P. Perdew, K. Burke, and M. Ernzerhof, Phys. Rev. Lett. **77**, 3865 (1996).
[58] H. J. Monkhorst and J. D. Pack, Phys. Rev. B **13**, 5188 (1976).
[59] N. Marzari and D. Vanderbilt, Phys. Rev. B **56**, 12847 (1997).
[60] Q. Wu, S. Zhang, H.-F. Song, M. Troyer, and A. A. Soluyanov, Computer Physics Communications **224**, 405 (2018).
[61] K. Momma and F. Izumi, Journal of Applied Crystallography **41**, 653 .
[62] R. Singha, A. K. Pariari, B. Satpati, and P. Mandal, Proceedings of the National Academy of Sciences **114**, 2468 (2017).
[63] A similar nodal structure has been reported recently in the rare-earth-trihalide YH_3[47]. The conduction and valence bands in YH_3 at Γ belong to A_{2u} and A_{2g} symmetries, respectively, with the crossing-point of nodal loops lying on the $\Gamma - A$ line.
[64] In general, these topological states can be related to the drumhead-like surface states associated with the nodal loops. However, in CaAuAs, it turns out that multiple nodal loops project over the same surface region and also overlap with the projected bulk bands in the absence of the SOC. As a result, the drumhead states are not clearly resolved, which makes it difficult to unambiguously correlate these states with the associated topological states in the Dirac semimetal. It will be interesting nevertheless to explore the evolution of drumhead states in CaAuAs along the lines of ZrPtGe[48].